Enhance Cold Adaptation of Bidomain Amylases via High-throughput Computational Engineering

Ning Ding, [1,†] Yaoyukun Jiang, [1,†] Robbie Ge,[1] Xinchun Ran,[1] and Zhongyue J. Yang[1-5,*]

[1]Department of Chemistry, Vanderbilt University, Nashville, Tennessee 37235, United States [2]Center for Structural Biology, Vanderbilt University, Nashville, Tennessee 37235, United States [3]Vanderbilt Institute of Chemical Biology, Vanderbilt University, Nashville, Tennessee 37235, United States [4]Data Science Institute, Vanderbilt University, Nashville, Tennessee 37235, United States [5]Department of Chemical and Biomolecular Engineering, Vanderbilt University, Nashville, Tennessee 37235, United State

Abstract

Cold-adapted bidomain enzymes are vital for transforming modern industries by decreasing energy consumption, delivering economic benefits, and fostering sustainability through reduced greenhouse gas emissions. Yet, the design strategies guiding their acquisition of cold adaptation remain unknown. Here, we developed an integrated computational-experimental strategy to engineer bidomain enzymes for enhanced cold-adaptation. Using five model amylase variants exhibiting different degrees of cold adaptation, we identified a descriptor from molecular dynamics simulations, namely domain separation index (DSI), which positively correlates with bidomain amylases' relative activity at 0°C. The bidomain amylase variants with a longer distance between its catalytic domain and carbohydrate-binding module (i.e., a high DSI) were observed to demonstrate cold adaptation. Guided by DSI, we developed a high-throughput molecular modeling protocol to convert the thermophilic

Pseudomonas saccharophila amylase (psA) into a cold-adapted bidomain enzyme, virtually screening 120 psA variants with different linkers. Two psA variants with a greater DSI value were selected and experimentally confirmed to be cold-adapted, with the psA121 variant achieving a 12-fold increase in relative activity at 0°C from 2.4% (specific activity: 14 U/mg) to 30.5% (specific activity: 219 U/mg). Conformational analyses reveal that compared to non-cold-adapted counterparts, cold-adapted variants leverage its linker to induce domain separation and enhance flexibility of active-site and binding loop via dynamic allostery, thereby promoting substrate recruiting, binding, and catalysis at lower temperatures. Statistical analyses of 120 variants demonstrate that helical motifs within linkers drive interdomain separation. Overall, our study offers strategies for engineering cold-adapted bidomain enzymes and suggests the molecular basis of cold adaptation in bidomain amylases.

Introduction

Biocatalytic cold adaptation, characterized by an enzyme's ability to maintain high catalytic activity at lower temperatures (e.g., 0°C to 25°C) [1-3], holds the potential for transforming modern industries [4]. Comprising 30%–40% of global industrial enzyme applications, cold-adapted proteases, lipases, amylases, and cellulases have revolutionized the laundry sector in low-temperature washing [5], textile sector in biopolishing [6], food industries in oligosaccharide and dairy production [7-8], and bioremediation sectors in polymer degradation [2, 9]. Additionally, cold-adapted enzymes provide solutions to minimizing industrial heating, thereby safeguarding heat-sensitive reactions [8, 10] and reducing greenhouse gas emissions [2, 4]. To underscore its impact, consider the starch industry, where eliminating the heating of 9

million tons of a 30% starch solution (~5% of yearly starch production) by 10°C, with an 80% efficient natural gas system, could result in a reduction of around 25.8 billion grams of CO_2 per year (**Text S1**). With an estimated global market value exceeding $750 million in 2023 (assuming 5% annual growth compound rate) [11], cold-adapted enzymes emerge not only as an economical choice but also as a driver for attaining sustainability in energy and the environment.

The pressing challenge is the lack of strategies for engineering enzymes, particularly bidomain enzymes, for enhanced cold adaptation [3, 12]. Bidomain enzymes occupy 60% of all enzyme classes, outnumbering single-domain enzymes threefold [13-14]. For example, amylases, constituting ~25% of the industrial enzyme market share [15], typically have a bidomain construct, featuring a catalytic domain (CD) for accelerating the reaction, a carbohydrate-binding module (CBM) for substrate recruitment, and a peptide linker connecting both domains. Structure-function relationship studies for single-domain enzymes have elucidated the association between enhanced conformational flexibility and cold adaptation, including local flexibility (e.g., active site residues [16-17], substrate binding loops [18-19], and surface loops [20-21]), global enzyme flexibility [8, 12], and hidden conformational states [22-23]. By installing a flexible loop in the active site, Meyer Cifuentes et al. converted a mesophilic polyethylene terephthalate hydrolase to a cold-adapted counterpart [2, 9]. However, bidomain enzymes differ significantly from single-domain enzymes because their interdomain interactions and mobilities can easily override conformational flexibilities within a single CD [24-25]. The peptide linkers, covalently bridging functional domains, also influence overall functions of the fused proteins [26-27]. In addition, bidomain enzymes pose more difficulties for structural characterization through

NMR due to their large size and through crystallography due to the high disorder and flexibility of their linker region. As such, despite their prevalence and industrial significance, the engineering principle for bidomain enzymes to acquire cold adaptation remains unknown [3, 12].

In this study, we developed an integrated computational-experimental strategy to engineer bidomain enzyme variants for enhanced cold adaptation. Using a thermophilic *Pseudomonas saccharophila* amylase (psA), a cold-adapted *Saccharophagus degradans* amylase (sdA), and their domain-swapping variants as model enzymes, we identified a molecular dynamics (MD) modeling-derived descriptor, domain separation index (DSI), to be linearly correlated with their experimentally measured relative activities at 0°C (i.e., the magnitude of cold adaptation), with cold-adapted bidomain enzymes showing a greater DSI value. We performed high-throughput computational screening over 120 psA variants with distinct linkers and found two psA variants, psA121 and psA475, with top-ranked DSI values. Both variants were characterized to be cold-adapted variants, with psA121 achieving a 12-fold increase in relative activity at 0°C from 2.4% (specific activity: 14 U/mg) to 30.5% (specific activity: 219 U/mg). MD analyses of psA121 elucidate the role of the linker in separating CD and CBM for promoting substrate recruitment, and in inducing dynamic fluctuation of the active-site loop in CD and substrate-binding loop in CBM for promoting substrate binding and catalysis via dynamic allostery. Eventually, statistical analyses for 120 variants demonstrate the significance of helical motifs to induce interdomain separation. Overall, this study offers practical strategies for engineering cold-adapted bidomain enzymes and elucidates the molecular basis of cold adaptation in bidomain amylases. These insights pave the way for rational design of enzymes with enhanced cold adaptation, potentially leading to significant advancements in industrial

87 biotechnology and sustainable bioprocesses.

88 **Results and Discussion**

89 **Domain separation index is a predictor for engineering cold-adapted bidomain amylases**

90 Enhanced flexibility has long been associated with the emergence of cold adaptation in
91 enzymes [12, 16-21]. However, a quantitative correlation between MD descriptors measuring
92 flexibility and the degree of cold adaptation (i.e., relative activity at lower temperatures
93 compared to optimal temperature) has remained elusive. Identifying such a molecular
94 descriptor will guide the engineering of cold-adapted amylases. Therefore, using five wild-type
95 and mutant amylases as model systems (**Figure 1A**), we investigated the correlation between
96 their degree of cold adaptation and MD descriptors that measure different facets of bidomain
97 enzyme flexibility, including conformational fluctuation (root mean square deviation, RMSD),
98 geometric compactness (radius of gyration, R_g), and interdomain separation (domain separation
99 index, DSI). Notably, DSI, a new descriptor proposed in this study, is calculated by subtracting
100 the sum of the R_g values of both domains from their geometric center distance (**Figure 1B**).
101 DSI evaluates the spatial proximity between both domains by mitigating the influence of
102 protein size.

103 The model enzymes involve sdA, psA, and three psA variants with domain swapping
104 (**Figure 1A**): psA-sp (psA's linker replaced by sdA's), psA-ps (psA's CBM replaced by sdA's),
105 and psA-ss (psA's linker and CBM replaced by sdA's). We experimentally assessed cold
106 adaptation in these five enzymes by comparing their activities at 0°C to their maximum
107 activities at 45°C (**Table S1**). Among the variants, psA, psA-sp, and psA-ps show less than

5.2% of their maximum activity at 0°C, indicating a lack of cold adaptation. In contrast, sdA and psA-ss retain 27.8% and 26.3% of their maximum activity at 0°C, respectively, demonstrating cold adaptation (**Figure 1C**).

Based on MD trajectories (5 × 200 ns, 0°C) simulated with AMBER [28], we computed RMSD, R_g, and DSI for sdA, psA and three psA variants (i.e., psA-sp, psA-ps, and psA-ss). No linear correlation was observed between the magnitude of cold adaptation and RMSD (Pearson correlation coefficient r: 0.23, Spearman correlation coefficient ρ: -0.10, **Figure 1C**). However, significant linear correlations were observed between cold adaptation and both R_g (r: 0.95, ρ: 0.90, **Figure 1C**) and DSI (r: 0.99, ρ: 1.00, **Figure 1C**). Both descriptors show that cold-adapted enzymes tend to be more "flexible", exhibiting an extended conformation with a greater R_g (sdA: 27.8 Å; psA-ss: 26.5 Å) and enhanced domain separation with a higher DSI (sdA: 8.9 Å; psA-ss: 8.5 Å). This observation supports the hypothesis that increased flexibility aids in cold adaptation. From non-cold-adapted (psA, psA-sp, and psA-ps) to cold-adapted amylases (sdA and psA-ss), R_g increases by merely 13.6% (24.5 Å to 27.8 Å), while DSI increases ~8.0-fold (1.0 Å to 8.9 Å). Thus, DSI demonstrates greater sensitivity to changes in cold adaptation.

DSI's numerical sensitivity originates from its ability to capture conformational states with varying interdomain interactions. To illustrate this point, we compared the time-evolution and distribution of DSI at 0°C in psA-ss (cold-adapted) and psA-sp (non-cold-adapted) (**Figure 1D** and **1E**). Both psA variants differ only in the source of CBM domains but involve distinct relative activities at 0°C (psA-ss: 26.3% vs. psA-sp: 0.9%) and DSI values (psA-ss: 8.5 Å vs.

psA-sp: 1.0 Å) (**Figure 1C**). During a typical 200 ns MD trajectory, the DSI of psA-ss fluctuates between 4 and 17 Å throughout the duration, averaging at 10.8 Å (**Figure 1D**), featuring a diverse population of extended conformational states (**Figure 1E**). In contrast, despite containing a small population of extended conformational states, psA-sp's DSI drops to -0.1 Å at 84.5 ns and remains below 0 Å (indicating domain overlaps) with minimal fluctuation (**Figure 1D**), which demonstrates the dominance of a compact conformational state (**Figure 1E**).

Compared to psA-sp, an enhanced interdomain separation in psA-ss prevents the two domains from interfering each other and improves CBM's accessibility to recruit polysaccharide substrate in solution [29]. Assuming that CBM can freely rotate around CD with the radius of DSI, psA-ss can cover a spherical volume of 2550 $Å^3$, which is 632 times greater than psA-sp, covering merely 4 $Å^3$. Due to its improved substrate accessibility, psA-ss likely maintains high activity in cold environments with limited substrate and water mobility [8]. Considering DSI's strong correlation with cold adaptation, numerical sensitivity to changes in cold adaptation, and physical relevance to conformational flexibility of bidomain enzymes, DSI will be used as a descriptor for guiding the engineering of cold-adapted bidomain amylases.

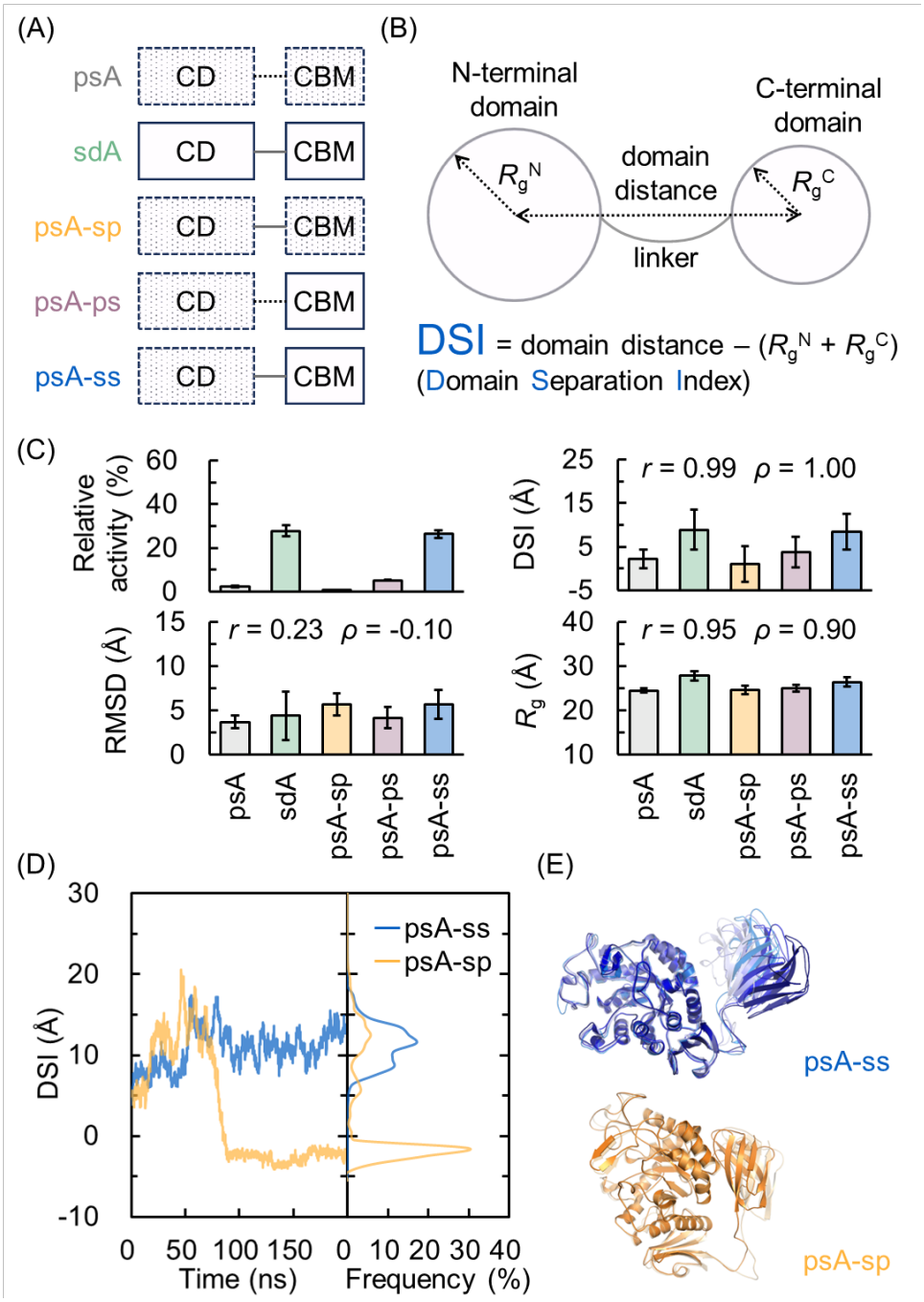

146

147 **Figure 1**. Comparative analysis of activity and molecular descriptors in psA, sdA, and psA

148 variants. (A) Structural composition of psA, sdA, and psA variants. (B) Schematic depicting

149 the definition of DSI. (C) Relative activity, DSI, RMSD and R_g for psA, sdA, and psA variants

150 at 0°C. Relative activity was quantified as the percentage ratio of enzymatic activity observed

151 at 0°C to that at the optimal temperature for the enzyme (45°C). DSI, RMSD and R_g are

obtained from MD simulations (5 × 200 ns, 0°C) using AMBER force field under a constant number of particles, volume, and temperature conditions with explicit water molecules. Data are presented as mean ± standard derivation. The linear regression equations are as follows: $y = 0.270x + 1.475$, $z = 0.016x + 4.551$, and $w = 0.101x + 24.437$, where x, y, z and w represent relative activity, DSI, RMSD and R_g, respectively. (D) Time evolution and distribution of DSI in a single 200 ns trajectory for psA-ss and psA-sp at 0°C. (E) Structural overlay of typical snapshots for psA-ss and psA-sp at 0°C.

Engineer mesophilic amylase psA for cold adaptation via high-throughput *in silico* screening of linker

Using DSI as a predictive descriptor, we set up a computational protocol with EnzyHTP [30-31], our high-throughput enzyme modeling software, to select psA variants with a strong likelihood for cold adaptation (**Figure 2A**). The protocol screens different peptide linkers that covalently bridge psA's CD and CBM domains, as engineering the linkers of bidomain enzymes (e.g., adjusting length, flexibility, and amino acid composition) has resulted in enhanced activity [32-34], expressibility [35], solubility [33], and stability [32, 34, 36]. Combining natural peptide linkers stored in LinkDB [37] and SynLinker databases [38], we created 3,528 psA variants (psA1—psA3528, **Supplementary spreadsheet S1**) and predicted their structures using AlphaFold2 [39]. These variants were categorized into four groups based on linker length (cutoff: 9 amino acids) and the presence of helical motifs (predicted by the DSSP method [40]), including: 1) short and helical, 2) short and non-helical, 3) long and helical, and 4) long and non-helical (**Supplementary spreadsheet S1**). We randomly selected 120 psA variants (30 per category)

and conducted 200 ns MD simulation at 0°C on each variant using EnzyHTP [30-31], aiming to identify the variants with an average DSI and standard deviation value above 8.5 and 2.6 Å, respectively (**Table S2**). Based on the regression model between DSI and relative activities (**Figure 1C**), exceeding this DSI threshold is estimated to maintain ~26.3% maximum activity at 0°C, featuring a cold-adapted psA variant. Out of the 120 psA variants, 10 demonstrate a DSI and standard deviation values exceeding the threshold and were selected to undertake a second round of 200 ns MD run (**Figure 2B** and **Table S3**). As a result, two variants, psA121 (DSI = 20.6±3.4 Å) and psA475 (DSI = 18.3±4.4 Å), were selected for experimental test (**Figure S1** and **S2**).

We expressed and purified psA121 and psA475, and characterized their activities at different temperatures ranging from 0°C to 75°C. Both psA121 and psA475 exhibit optimal hydrolytic activities at 45°C (**Figure 2C** and **Figure S5**), the same as the wild-type psA. Consistent with our computational prediction, both psA121 and psA475 demonstrate cold adaptation. At 0°C, psA121 and psA475 retain 30.5% and 20.1% of their maximum activities, which, compared to the wild-type psA, enhance the relative activities by 11.5-fold and 7.2-fold, respectively. At 25°C, psA121 and psA475 retain 78.1% and 65.8% of their maximum activities, respectively, which are 1.7-fold and 1.2-fold higher than those of the wild-type psA (**Figure 2D**). These results show that high-throughput *in silico* screening of interdomain linkers with a high DSI is an effective strategy for converting mesophilic to cold-adapted bidomain amylases. This approach differs from single-domain enzyme engineering, which achieves cold adaptation by increasing the flexibility of active-site and surface loops [18-19, 41].

Unexpectedly, psA121 shows both enhanced cold adaptation and increased activity at high temperatures compared to wild-type psA. psA121 retains 29.4% of its maximum activity at 75°C (**Figure 2C**), in sharp contrast to sdA, the native cold-adapted amylase, which rapidly loses activity above its optimal temperature (45°C) and becomes completely inactive at 75°C. To our knowledge, amylases with broader temperature adaptation across 75°C have rarely been reported [42-43]. Cold-adapted enzymes typically show reduced activity and stability at high temperatures compared to their mesophilic counterparts [1, 44-45]. Due to its broader temperature adaptation, psA121 holds a great potential for industrial applications due to its cooperation with other enzymes for use in a diverse range of working temperatures in cascade reactions [46-47].

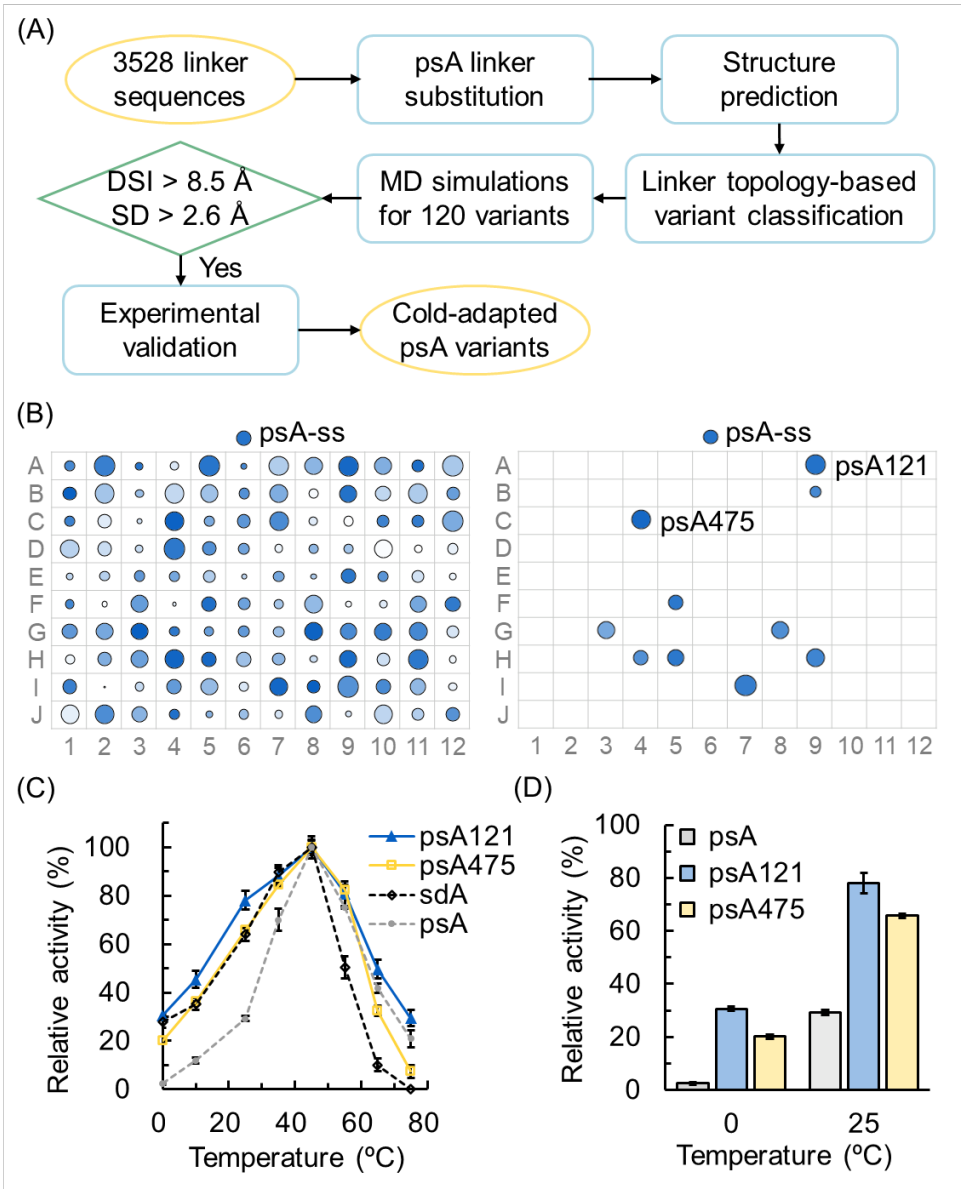

204

205 **Figure 2**. Identification of cold-adapted psA variants through high-throughput screening of
206 linker. (A) Workflow for identifying cold-adapted psA variants by integrating computational
207 and experimental methods. We created 3,528 psA variants (psA1–psA3528) by replacing psA's
208 native linker with sequences from the LinkDB and SynLinker databases. The structures of these
209 variants were predicted using AlphaFold2, and the secondary structure within the linker region
210 was analyzed using the DSSP method. The variants were categorized into four groups based
211 on linker topology, focusing on linker length and the presence of a helix. We randomly selected

30 variants from each group, totaling 120 variants, and performed MD simulations at 273.15 K. Variants with an average DSI exceeding 8.5 Å and a DSI standard deviation above 2.6 Å across two MD runs were selected for further experimental validation to confirm their cold adaptation. (B) Average DSI and standard deviation for psA variants. Variants are plotted as circles in a 12 × 10 matrix, with their corresponding coordinates, average DSI, and standard deviation values listed in **Tables S3** and **S4**. The size of each circle represents the average DSI, with larger circles indicating higher DSI values. The darkness of each circle represents the standard deviation of the DSI, with darker circles indicating higher standard deviations. psA-ss is used as a reference, with average DSI and standard deviation values above 8.5 Å and 2.6 Å, respectively. In the first round of MD simulations for the 120 variants (left), 10 variants show average DSI and standard deviation values above 8.5 Å and 2.6 Å, respectively. In the second round of MD simulations for these 10 variants (right), two variants (psA121 and psA475) meet the same DSI criteria. (C) Relative activities of psA121, psA475, sdA and psA at temperatures ranging from 0°C to 75°C. (D) Relative activities of psA, psA121 and psA475 at 0°C and 25°C. Relative activity is quantified as the percentage ratio of enzymatic activity observed at the specified assay temperature to that at the optimal temperature for the enzyme. Data are shown as mean ± standard deviation.

Linker-mediated domain separation induces dynamic allostery to enhance flexibility of the active-site loop in CD and the binding loop in CBM

In prior sections, we demonstrated domain separation index (DSI) as a predictor for cold adaptation in bidomain amylases. By adopting the linkers that increase the DSI between the

CD and CBM at 0°C, we experimentally converted thermophilic psA into two cold-adapted variants (psA121 and psA475). In particular, psA121 exhibits a 7.8-fold higher DSI (5 × 200 ns MD runs) and a 12.5-fold higher relative activity than psA at 0°C. However, it remains unclear how changing the linker influences the CD and CBM, thereby enhancing the psA121's capability of substrate recruiting, binding, and catalysis at lower temperatures. For single-domain enzymes, cold adaptation is hypothesized to arise from increased structural flexibility in either the active site region [16-17, 19, 48-53] or the surface region [20-21, 41, 44, 54-57]. Therefore, using psA121 as a model, we compared the root-mean-square fluctuation (RMSF) values of its CD and CBM residues with those of psA (**Figure 3A** and **Figure 4A**).

Compared with psA, psA121 shows significantly increased flexibility in both the surface loop (L387–S403, colored in red, **Figures 3A** and **3B**) and active-site loop (F289–R316, colored in green, **Figures 3A** and **3B**), exhibiting a 1.3-fold and 2.2-fold increase in RMSF, respectively (**Tables 1** and **S6**). These results align with prior studies indicating that cold-adapted enzymes exhibit greater flexibility in their active-site and surface loops compared to their mesophilic counterparts [16-17, 48-53]. However, a notable distinction in our work is that most existing cold-adapted enzyme variants involve mutations in the CD [18-19, 41], whereas psA121 maintains an identical CD sequence to psA, differing only in the linker region that is ~30 Å away from the active site and surface loops.

To investigate the structural basis of linker-induced dynamic allostery in CD, we compared H-bonding patterns in psA and psA121, emphasizing the CD-CBM interface, the surface loop L387–S403, and the active-site loop F289–R316. In psA, the CD-CBM complex prefers a

compact conformation with a low DSI value (e.g., DSI = -0.4 Å exemplified in **Figure 3C**), featuring the formation of multiple pairs of inter-domain H-bonds at the CD-CBM interface, including S364-G461, S364-N462, F365-S464, F365-S467 and S377-S458 (**Figure S3**). Among these pairs, F365 resides in an interface loop (F365–G371, colored in purple, **Figure 3C**) that interacts strongly with the surface loop (in green) via three H-bonds (i.e., Y369-Q396, S370-S389, S370-D390), thereby limiting the mobility of the surface loop [58-59]. In psA121, the CD and CBM domains are physically spaced by the rigid α-helical linker (colored in blue, **Figure 3D**), leading to an extended conformation with broken inter-domain H-bonding interactions at the CD-CBM interface (e.g., DSI > 10 Å in all MD snapshots, exemplified in **Figure S1**). The disruption of H-bonding networks mobilizes the surface loop (in green) and reorients the surface loop to interact with the active-site loop (in red) through an H-bond between R316 and V397 (**Figure 3E**). The interaction is characterized by a broad distribution of R316–V397 distance over 8 Å, with the active-site loop switching to an open state for substrate binding as the R316–V397 H-bond is on, and a closed state for catalysis as the R316–V397 H-bond is off (**Figure 3F**). Induced by the mobile surface loop, the active-site loop in psA121 is capable of quickly recruiting the substrate for binding and orienting the substrate in a conformation favoring the reaction through the catalytic residue D294 [60-63] at lower temperatures, instead of populating dominantly in one state like psA (**Figure S3**).

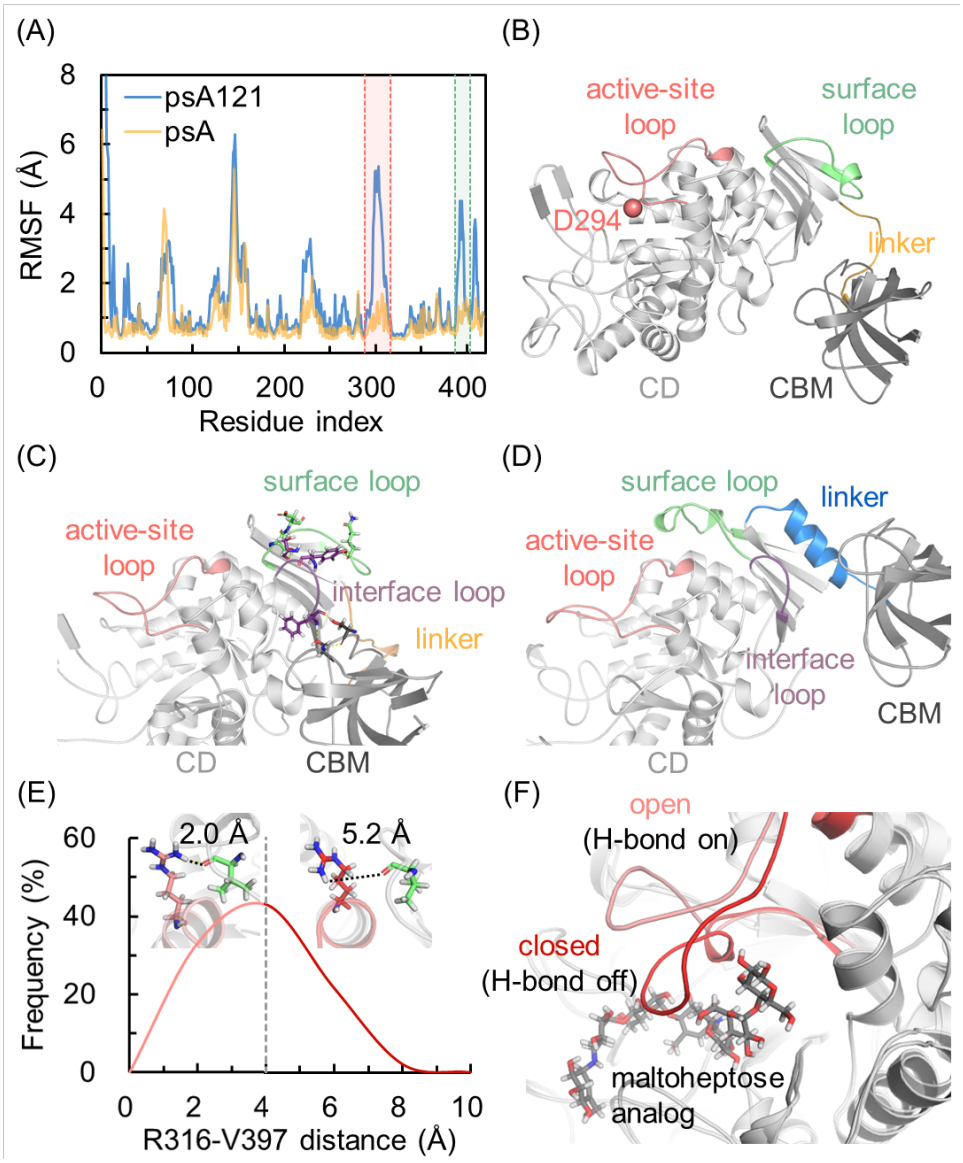

272

273 **Figure 3**. Effects of linker on interdomain separation and flexibility of CD. (A) RMSF of
274 residues within the CD of psA and psA121. Two loop regions in psA121 involve significant
275 increases in flexibility compared to psA, including Loop F289–R316 (active-site loop, colored
276 in red) and Loop L387–S403 (surface loop, colored in green). (B) Structure of psA highlighting
277 the active-site loop (F289–R316, colored in red) and surface loop (L387–S403, colored in
278 green). The catalytic residue D294 is shown as a red sphere. (C) Conformation of a typical
279 snapshot of psA, highlighting the active-site loop (F289–R316, colored in red), surface loop
280 (L387–S403, colored in green), interface loop (F365–G371, colored in purple), and linker

(G419–L433, colored in orange). The interface loop interacts with the surface loop via three H-bonds (i.e., Y369-Q396, S370-S389, S370-D390). (D) Conformation of a typical snapshot of psA121, highlighting the active-site loop (F289–R316, colored in red), surface loop (L387–S403, colored in green), interface loop (F365–G371, colored in purple), and linker (A419–G434, colored in blue). (E) The distribution of distances between the oxygen atom of residue V397 and the hydrogen atom of residue R319. Distances less than 4 Å are shown in pale red, indicating the formation of hydrogen bonds, while distances greater than 4 Å are shown in dark red, indicating no hydrogen bond formation. The gray dashed line marks the threshold distance of 4 Å. (F) Conformations of typical snapshots of psA121 in complex with maltoheptaose analog. The open and closed conformation of the active-site loop are shown in pale red and dark red, respectively. The ligand is localized by aligning the CD (D1–S418) of the psA121 structures with that of the psA crystal structure (PDB ID: 6JQB) [60] using the command "align" in PyMOL.

We further investigated the change of conformational flexibility in CBM. Compared to psA, psA121's CBM exhibits significantly enhanced flexibility in the binding loop (T445–S450, colored in pink, **Figures 4A** and **4B**), and in residues N500 and E501 (colored in green, **Figure 4B**), both showing a one-fold increase in RMSF (**Tables 1** and **S6**). We further compared H-bonding patterns in the CBM of psA and psA121, focusing on the CD-CBM interface, the binding loop, and residues N500 and E501. In psA, R470, located within the interface loop (N456–R470, colored in purple, **Figure 4C**), forms an H-bond with E501, whose adjacent residue N500 restricts the motion of the binding loop via two H-bonds (i.e., E501-G448 and N500-D449). In psA121, the separation of CD and CBM domains (**Figure S3**)

destructs the H-bonding networks observed within the CBM (**Figure 4D**), increasing the mobility of the binding loop.

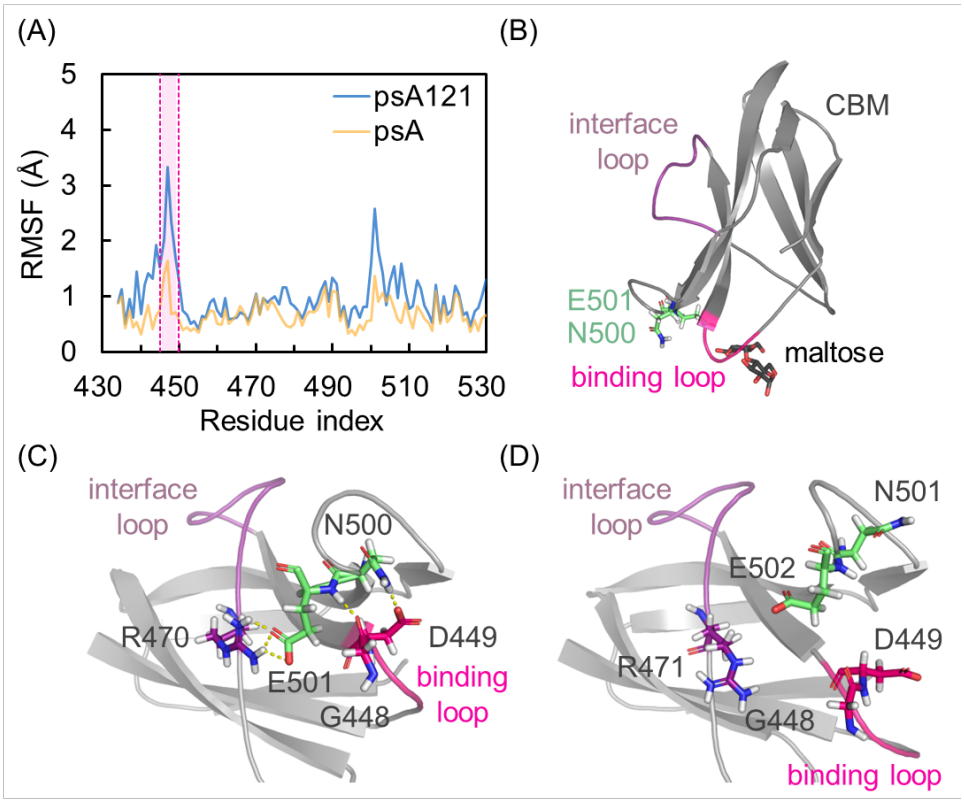

Figure 4. Effects of linker on the flexibility of CBM. (A) RMSF of residues within the CBM of psA and psA121. Loop T445–S450 (binding loop, colored in pink) in psA121 involves a significant increase in flexibility compared to psA. (B) Structure of psA highlighting the interface loop (N456–R470, colored in purple), binding loop (T445–S450, colored in pink), and residues N500 and E501 (shown as green sticks). The ligand is localized by aligning the CBM (V434–F530) of the psA structure with that of the crystal structure of *Bacillus circulans* cyclodextrin glycosyltransferase (PDB ID: 1CDG) [64] using the command "align" in PyMOL. (C) Conformation of a typical snapshot of psA, highlighting the interface loop (N456–R470, colored in purple) and binding loop (T445–S450, colored in pink). Residue R470 in the interface loop forms H-bonds with residue E501. Residues E501 and N500 interact with the

316 binding loop via two H-bonds (i.e., E501-G448 and N500-D449). (D) Conformation of a
317 typical snapshot of psA121, highlighting the interface loop (N457–R471, colored in purple)
318 and binding loop (T446–S451, colored in pink).

319 Besides psA121, the enhancement of functional loop flexibility is also observed in the
320 cold-adapted amylase variant, psA475, which involves a 1.9-fold and 1.1-fold increase in
321 RMSF for the active-site loop and binding loop, respectively, compared to psA (**Table 1**). In
322 contrast, the non-cold-adapted variant, psA-sp, shows similar magnitude of flexibility in the
323 active-site loop (RMSF = 0.9 Å) and binding loop (RMSF = 1.1 Å) to that of psA. Based on
324 the four variants (psA, psA121, psA475, and psA-sp), which share identical CD and CBM but
325 differ in linker sequences, we note a convergent trend that the cold-adapted linkers (psA121
326 and psA475) enhance the flexibility of functional loops in CD and CBM while promoting
327 domain separation (**Table 1**).

328 **Table 1.** DSI, relative activity at 0°C, and root mean square of RMSF values for the residues
329 composing the active-site loop and binding loop for psA, psA121, psA475 and psA-sp.

psA variants	DSI (Å)[1]	Relative activity at 0°C (%)[2]	RMSF (Å)[3]	
			Active-site loop (F289–R316)	Binding loop (T445–S450)
psA	2.1±2.2	2.4±0.5	1.0	1.0
psA121	16.6±5.9	30.5±0.8	3.1	2.1
psA475	15.7±9.1	20.1±0.7	2.9	2.2
psA-sp	1.0±4.1	0.9±0.0	0.9	1.1

330 [1] DSI values are obtained from MD simulations at 0°C (5 × 200 ns). Data are shown as mean
331 ± standard derivation. [2] Relative activity was quantified as the percentage ratio of enzymatic
332 activity observed at 0°C to that at the optimal temperature for the variants (45°C). Data are
333 shown as mean ± standard derivation (three replica). [3] Root mean square of RMSF values for

the residues composing the active-site loop and binding loop. Data are obtained from MD simulations at 0°C (5 × 200 ns). The residue index for the binding loop is based on the wild-type psA. The corresponding indices for the binding loop in psA121, psA475, and psA-sp are T446–S451, T440–S445, and T448–S453, respectively.

It was generally believed that an optimal enzyme should be "flexible but not too flexible" and "rigid but not too rigid" [65-66]. Why does an increased active-site and binding loop flexibility benefit catalysis under cold conditions despite its potential entropy cost? As an intuitive explanation, we would note that the substrates of amylases are oligo- and polysaccharides, which are long and bulky, presenting a non-trivial barrier to the substrate recruiting and binding at lower temperatures. The open conformation of the active-site loop facilitates the binding of bulky substrates, while the closed conformation enhances catalysis by shielding solvents and increasing the amylases' enthalpic interactions with the substrate. Maintaining the flexibility of the active-site loop is crucial for the enzyme to quickly position a single polysaccharide chain into its active-site for hydrolytic cleavage, thereby sustaining a high turnover rate at lower temperatures (**Figure 5**). CBM, on the other hand, leverages its flexible binding loop to rapidly separate starch chains, slide along a single polysaccharide chain for CD to bind, and facilitate product release [67]. This synergistic effect of increased flexibility in both the CD active-site loop and the CBM binding loop contributes to the cold adaptation of amylases (**Figure 5**).

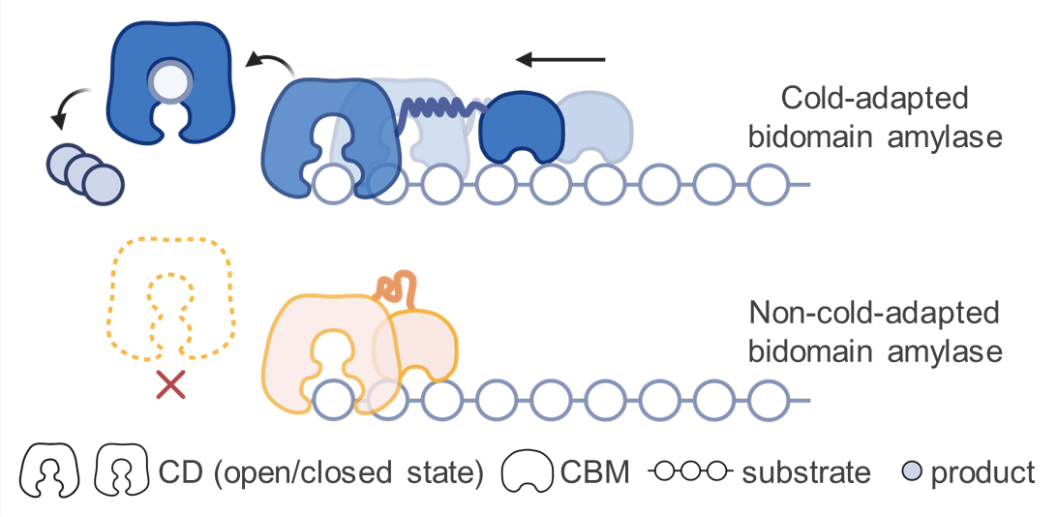

Figure 5. Illustration showing how a greater magnitude of domain separation between CD and CBM enhances cold adaptation in a bidomain enzyme by influencing the conformational flexibility and dynamic allostery of the individual domains.

The increase in flexibility of both the active-site loop in CD and the binding loop in CBM can be achieved by adopting a linker that enhances domain separation. Compared to engineering the individual domains separately, engineering linkers—a single non-catalytic component—is easier for structure design and plasmid construction. The subsequent question is, which linker types serve as effective spacers to enhance domain separation? Based on the MD trajectory data of 120 psA variants with different linkers (**Table S2**), we investigated the linker characteristics that mediate interdomain separation between the CD and CBM. In particular, we focused on linker length and the presence of helices, two factors that have been widely proposed to correlate with the magnitude of interdomain separation [27, 68]. We categorized the linkers into short and long groups (60 variants each) with the short group having an average sequence length of 6.7±1.6 and the long group 15.3±4.6 (**Table S7**). We observed similar DSI distributions in both groups (**Figure 6A**): the median DSI is 5.5±1.0 Å for the

short-linker group and 6.8±1.1 Å for the long-linker group, with mean DSIs of 7.4±1.0 Å and 8.2±1.1 Å, respectively (**Table S7**). The similarity of DSI distribution indicates that sequence length has minimal influence on the magnitude of domain separation. On the other hand, the presence of helices significantly impacts the magnitude of interdomain separation (**Figure 6B**). Linkers with a helical motif (60 variants) exhibit a median DSI of 8.2±1.1 Å, which is 4.7 Å greater than those without a helical motif (3.6±0.9 Å) (**Table S7**). A 4.7 Å increase in DSI is estimated to enhance the relative activity by ~20% at 0°C (**Figure 1C**), indicating the role of helical motifs as a spacer to enlarge the distance between CD and CBM for cold adaptation. This trend is also reflected in the mean DSI values (helical linkers: 9.2±1.1 Å vs non-helical linkers: 6.4±0.9 Å, **Table S7**). In addition to psA121, helical linkers have been observed in other cold-adapted enzymes, such as Atlantic salmon trypsin [68], *Vibrio* sp. alginate lyase [69], and *Pseudomonas* sp. phosphoglycerate kinase [70]. Although the focus of this work is on cold adaptation, the presence of helical motif helps understand psA121's enhanced thermal adaptation at 75°C. While higher temperatures benefit the reaction kinetics by making reactive conformations more thermally accessible, they also cause misorientation between CD and CBM and partial unfolding of each domain, leading to diminished enzyme activity. The helical linker in psA121 maintains the relative orientation between CD and CBM, serving as a shaft to support the structural integrity of the bidomain enzyme.

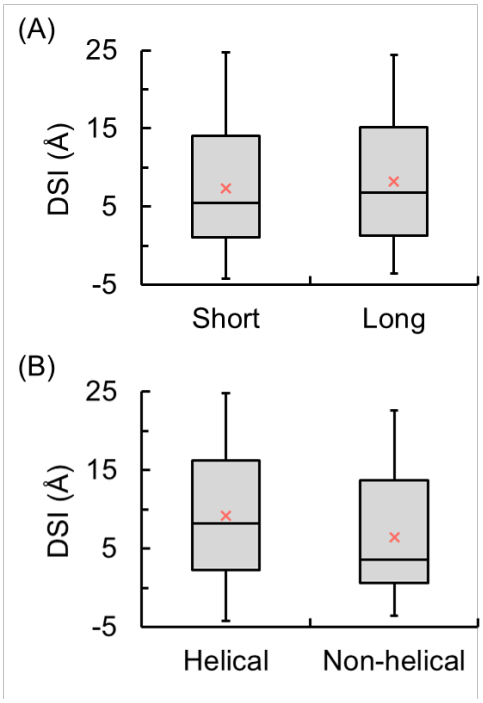

Figure 6. Effects of linker length and the presence of helical motifs on interdomain separation. (A) DSI for psA variants with short and long linkers. Linkers longer than 9 amino acids are categorized as "long" and the rest as “short”. (B) DSI for psA variants with and without helical motifs. Linkers with a secondary structure featuring a 3-10 helix, α-helix, or π-helix are categorized as “helical”, and the rest as “non-helical”.

Conclusion

In conclusion, this study presents an integrated computational-experimental approach for engineering cold-adapted bidomain enzymes. We identified the domain separation index (DSI), derived from MD modeling, as a predictive descriptor of cold adaptation in amylases. Using DSI-guided high-throughput computational screening, we successfully generated two psA variants with enhanced cold adaptation. Notably, psA121 exhibited a 12-fold increase in relative activity at 0°C, from 2.4% to 30.5% (specific activity from 14 U/mg to 219 U/mg).

Molecular dynamics analyses show that the cold-adaptation-inducing linkers, besides promoting greater domain separation between CD and CBM to prevent mutual interference, enhance the flexibility of the active-site loop in CD and the binding loop in CBM to favor substrate recruiting, binding, positioning, and catalysis at low temperatures. Eventually, statistical analyses of DSI for 120 psA variants highlight the importance of helical motifs in linkers for enhancing interdomain separation. Our work established a strategy for engineering cold-adapted bidomain enzymes, paving new ways for creating cold-adapted enzymes for sustainable industrial biocatalysis.

Methods

Protein Structure Preparation

This study involves two wild-type enzymes: *Saccharophagus degradans* amylase (sdA), and *Pseudomonas saccharophila* amylase (psA). Three psA variants were engineered through domain swapping: psA-sp (psA's linker replaced by sdA's), psA-ps (psA's CBM replaced by sdA's), and psA-ss (psA's linker and CBM replaced by sdA's). We predicted the structures of the wild-type and variant enzymes using AlphaFold2 [39] via the ColabFold server (version 1.5.3) [71]. The sequences and parameters used for the prediction are listed in **Tables S8** and **S9**, respectively.

The predicted structures were prepared for MD simulations with the AMBER19 *tleap* tool[72]. The AMBER ff14SB force field[73] was applied. All missing heavy atoms were added using *tleap*. The coordinate of hydrogens and protonation states of titratable residues in the proteins was determined by the *get_protonation()* function using EnzyHTP software[30-31],

which uses PDB2PQR[74] and PROPKA3[75]. The disulfide bonds were identified by PDB2PQR and constructed using the bond command of *tleap*, which was also automated by EnzyHTP (**Text S2**).

Molecular Dynamics Simulations

We performed MD simulations for sdA, psA and psA variants using the AMBER19 software package [72]. The SHAKE algorithm [76] was used to constrain all hydrogen-containing bonds. The enzyme was then solvated in a periodic truncated octahedron box with a 10 Å buffer of TIP3P water and was neutralized with Na^+ counterions.

For each enzyme, we optimized the solvated system using the steepest descent method for 10,000 steps followed by the conjugate gradient method for another 10,000 steps. After minimization, we heated the water box from 0 K to the designated temperature (273.15 K) within 36 ps with constant volume, equilibrated it for 4 ps under an NVT condition, and further equilibrated for additional 1 ns. The Langevin thermostat was used to control the temperature [77]. In addition, we restrained the backbone C_α, C, and N of the amide group with a weight of 2 $kcal \cdot mol^{-1} \cdot Å^{-2}$ from minimization to equilibration. After equilibration, we conducted production runs at constant volume and temperature for 210 ns and output the trajectories every 100 ps. The snapshots from the last 200 ns of the production run were used for analyses, resulting in a total of 2,000 snapshots for each production run. All simulations were performed with a time step of 2 fs. Five parallel simulations (5 × 200 ns) were conducted each for sdA, psA, and psA variants (i.e., psA-sp, psA-ps, psA-ss and psA121).

Molecular Dynamics Trajectory Analysis

Five parameters, including RMSD, domain distance, R_g, DSI, and RMSF were computed based on the MD trajectory data using the *cpptraj* tool in AMBER [28]. The mean values for each parameter of sdA, psA and psA variants (psA-sp, psA-ps, psA-ss, and psA121) were calculated based on 5 replicas of MD run (5 × 2,000 snapshots). Domain annotation of sdA and psA, detailing which sequence regions correspond to the CD, linker, and CBM domains, was based on previous studies [8, 60] with sequences provided in **Table S7**. The mass-weighted RMSD was calculated by including backbone heavy atoms (i.e., Cα and C, O, and N in the amide group) with reference to the input structure of the MD simulation. The R_g was calculated for the N-terminal domain (R_g^N), the C-terminal domain (R_g^C), and the entire structure (R_g), considering all heavy atoms. The domain distance was calculated as the distances between the geometric centers of CD and CBM, considering all heavy atoms. DSI was calculated as the domain distance minus the sum of the radius of gyrations for each domain of the enzyme [DSI = domain distance – (R_g^N + R_g^C)]. Mass-weighted RMSF for psA, psA121, psA475, and psA-sp was calculated using all heavy atoms, based on trajectories where each snapshot was aligned to the average structure of the CD and the CBM.

High-throughput Linker Screening

We generated 3,528 psA variants (psA1–psA3528) by replacing psA's native linker with sequences obtained from the LinkDB [37] and SynLinker databases [38]. The linker sequences are shown in **Supplementary Spreadsheet S1.** We predicted the structures of these psA variants using AlphaFold2 [39], and determined the secondary structure within the linker region using *cpptraj* [28] with the Defining Secondary Structure of Proteins (DSSP) [40] method

(**Supplementary Spreadsheet S1**). We classified psA variants based on their linker topology, emphasizing linker length and the presence of helical motifs. With an average linker length of 9.2 amino acids over 3528 linkers, we classified linkers longer than 9 amino acids as "long" and the rest as “short”. Linkers with a secondary structure featuring a 3-10 helix, α-helix, or π-helix were categorized as “helical”, and the rest as “non-helical”. Using these two criteria, we grouped the psA variants into four categories: 1) short and helical, 2) short and non-helical, 3) long and helical, and 4) long and non-helical. We randomly selected 30 variants from each group, totaling 120 variants (**Table S2**), and conducted a single replica MD run for each at 273.15 K. The variants with an average DSI exceeding 8.5 Å and a DSI standard deviation above 2.6 Å were selected for a second MD run (10 in total provide the number of variants filtered in from the first round). Under the same DSI criteria, two variants (psA121 and psA475) were identified. These two variants were expressed and purified for enzyme activity assays at different temperatures.

Bacterial Strains, Plasmids and Cloning

Genes encoding sdA, psA and psA variants (psA-sp, psA-ps, psA-ss, psA121, and psA475) were synthesized by Integrated DNA Technologies (Morrisville, NC). We amplified the synthesized genes through polymerase chain reaction using Q5 High-Fidelity Master Mix (New England Biolabs). We assembled the amplified genes and pET-22b vector using Gibson Assembly Master Mix (New England Biolabs). We transformed the recombinant plasmids into *Escherichia coli* JM109 and *E. coli* BL21 for DNA manipulations and protein expression, respectively.

Protein Expression and Purification

A single colony from the transformed cells was inoculated into Luria-Bertani medium (5 mL) supplemented with ampicillin (50 μg mL^{-1}) and grown at 37°C overnight with agitation at 220 rpm. The overnight culture (2 mL) was then inoculated into Terrific-Broth medium (200 mL) supplemented with ampicillin (50 μg mL^{-1}). The culture was incubated at 30°C with agitation at 160 rpm for 72 hours. After incubation, the cells were removed by centrifugation at 10,000 × g for 30 minutes at 4°C, and the supernatant, which contained crude enzymes, was collected for purification.

To purify the enzymes, the concentrated supernatant (20 mL) was mixed with 5 mL of Ni-NTA resin (Invitrogen) in buffer A (10 mM Tris-HCl, and 300 mM NaCl, pH 7.5). The mixture was incubated under rotation overnight at 4°C. The resin was then washed with buffer B (10 mM Tris-HCl, 300 mM NaCl, and 20 mM imidazole, pH 7.5) to eliminate non-target proteins. The target proteins were eluted with buffer C (10 mM Tris-HCl, 300 mM NaCl, and 250 mM imidazole, pH 7.5). The purified proteins were dialyzed in buffer D (10 mM Tris-HCl, pH 7.0) at 4°C for 24 hours and analyzed by sodium dodecyl sulfate-polyacrylamide gel electrophoresis.

Thermal Adaptation Characterization

The hydrolytic activities of amylases were measured by determining the reducing sugars released from the hydrolysis of starch using the 3,5-dinitrosalicylic acid (DNS) method [78]. The reaction mixture containing 0.2 mL of the enzyme and 1.8 mL of 1% (w/v) soluble starch (Fisher Scientific) in Buffer D was incubated at temperatures ranging from 0°C to 75°C. After 15 minutes, the reaction was quenched by adding 2 mL of DNS reagent and boiled for 5 min.

The absorbance was measured at 540 nm. One unit of hydrolytic activity was defined as the quantity of enzyme that released reducing sugar equivalent to one μmol of glucose per minute under the assay conditions. Relative activity was quantified as the percentage ratio of enzymatic activity observed at the specified assay temperature to that at the optimal temperature for the enzyme. Three biologically independent replicates were used to calculate mean and standard derivation.

ASSOCIATED CONTENT

Supporting Information. Figures S1–S4, Text S1–S2, and Tables S1–S9. (PDF)

Data Availability The AlphaFold-predicted structures, MD simulation input files, and original data spreadsheets are openly available on Zenodo: 10.5281/zenodo.12095218.

AUTHOR INFORMATION

Corresponding Author

*Email: zhongyue.yang@vanderbilt.edu phone: 615-343-9849

Notes

The authors declare no competing financial interest.

Author Contributions

ND and ZY designed the study. ND conducted the experiments. ND, YJ, and RG performed MD simulations and gathered computational data. ND and XR predicted the structures. ND, YJ, and ZY wrote the manuscript.

Acknowledgement

This research was supported by the startup grant from Vanderbilt University. Z. J. Yang, N. Ding, and Y. Jiang are supported by the National Institute of General Medical Sciences of the National Institutes of Health under award number R35GM146982. Z. J. Yang thanks the sponsorship from Rosetta Commons Seed Grant Award and the Dean's Faculty Fellowship in the College of Arts and Science at Vanderbilt. This work used SDSC Dell Cluster with AMD Rome HDR IB at Expanse from the Advanced Cyberinfrastructure Coordination Ecosystem: Services & Support (ACCESS) program, which is supported by National Science Foundation grants BIO200057. [79]

References

1. Feller, G.; Gerday, C., Psychrophilic enzymes: Hot topics in cold adaptation. *Nature Reviews Microbiology* **2003,** *1* (3), 200-208.
2. Liu, Y.; Jia, K.; Chen, H.; Wang, Z.; Zhao, W.; Zhu, L., Cold-adapted enzymes: Mechanisms, engineering and biotechnological application. *Bioprocess and Biosystems Engineering* **2023,** *46* (10), 1399-1410.
3. Nowak, J. S.; Otzen, D. E., Helping proteins come in from the cold: 5 burning questions about cold-active enzymes. *BBA Advances* **2023**, 100104.
4. Kumar, A.; Mukhia, S.; Kumar, R., Industrial applications of cold-adapted enzymes: Challenges, innovations and future perspective. *3 Biotech* **2021,** *11* (10), 426.
5. Al-Ghanayem, A. A.; Joseph, B., Current prospective in using cold-active enzymes as eco-friendly detergent additive. *Applied Microbiology and Biotechnology* **2020,** *104* (7), 2871-2882.
6. Bhat, A.; Riyaz-Ul-Hassan, S.; Ahmad, N.; Srivastava, N.; Johri, S., Isolation of cold-active, acidic endocellulase from Ladakh soil by functional metagenomics. *Extremophiles* **2013,** *17*, 229-239.
7. Chen, Q.; Wu, Y.; Huang, Z.; Zhang, W.; Chen, J.; Mu, W., Cold-active enzymes in the dairy industry: Insight into cold adaption mechanisms and their applications. *Trends in Food Science & Technology* **2022,** *125*, 126-135.
8. Ding, N.; Zhao, B.; Ban, X.; Li, C.; Venkataram Prasad, B.; Gu, Z.; Li, Z., Carbohydrate-binding module and linker allow cold adaptation and salt tolerance of maltopentaose-forming amylase from marine bacterium *Saccharophagus degradans* 2-40 T. *Frontiers in Microbiology* **2021,** *12*, 708480.
9. Meyer Cifuentes, I. E.; Wu, P.; Zhao, Y.; Liu, W.; Neumann-Schaal, M.; Pfaff, L.; Barys, J.; Li, Z.; Gao, J.; Han, X., Molecular and biochemical differences of the tandem and cold-adapted PET hydrolases Ple628 and Ple629, isolated from a marine microbial consortium. *Frontiers in Bioengineering and Biotechnology* **2022,** *10*, 930140.

10. Wang, Z.-P.; Cao, M.; Li, B.; Ji, X.-F.; Zhang, X.-Y.; Zhang, Y.-Q.; Wang, H.-Y., Cloning, secretory expression and characterization of a unique pH-stable and cold-adapted alginate lyase. *Marine Drugs* **2020,** *18* (4), 189.
11. Gerday, C.; Aittaleb, M.; Bentahir, M.; Chessa, J.-P.; Claverie, P.; Collins, T.; D'Amico, S.; Dumont, J.; Garsoux, G.; Georlette, D., Cold-adapted enzymes: From fundamentals to biotechnology. *Trends in Biotechnology* **2000,** *18* (3), 103-107.
12. Tindbaek, N.; Svendsen, A.; Oestergaard, P. R.; Draborg, H., Engineering a substrate-specific cold-adapted subtilisin. *Protein Engineering Design and Selection* **2004,** *17* (2), 149-156.
13. Apic, G.; Gough, J.; Teichmann, S. A., Domain combinations in archaeal, eubacterial and eukaryotic proteomes. *Journal of Molecular Biology* **2001,** *310* (2), 311-325.
14. Redfern, O. C.; Harrison, A.; Dallman, T.; Pearl, F. M. G.; Orengo, C. A., CATHEDRAL: A fast and effective algorithm to predict folds and domain boundaries from multidomain protein structures. *PLoS Computational Biology* **2007,** *3* (11), e232.
15. De Souza, P. M.; de Oliveira Magalhães, P., Application of microbial α-amylase in industry – A review. *Brazilian Journal of Microbiology* **2010,** *41* (4), 850.
16. D'Amico, S.; Sohier, J.; Feller, G., Kinetics and energetics of ligand binding determined by microcalorimetry: Insights into active site mobility in a psychrophilic α-amylase. *Journal of Molecular Biology* **2006,** *358* (5), 1296-1304.
17. Lonhienne, T.; Gerday, C.; Feller, G., Psychrophilic enzymes: Revisiting the thermodynamic parameters of activation may explain local flexibility. *Biochimica et Biophysica Acta (BBA) - Protein Structure and Molecular Enzymology* **2000,** *1543* (1), 1-10.
18. Huang, A.; Lu, F.; Liu, F., Exploring the molecular mechanism of cold-adaption of an alkaline protease mutant by molecular dynamics simulations and residue interaction network. *Protein Science* **2023**, e4837.
19. Blázquez-Sánchez, P.; Vargas, J. A.; Furtado, A. A.; Griñen, A.; Leonardo, D. A.; Sculaccio, S. A.; Pereira, H. D. M.; Sonnendecker, C.; Zimmermann, W.; Díez, B., Engineering the catalytic activity of an Antarctic PET-degrading enzyme by loop exchange. *Protein Science* **2023,** *32* (9), e4757.
20. Åqvist, J.; Isaksen, G. V.; Brandsdal, B. O., Computation of enzyme cold adaptation. *Nature Reviews Chemistry* **2017,** *1* (7), 0051.
21. Isaksen, G. V.; Åqvist, J.; Brandsdal, B. O., Protein surface softness is the origin of enzyme cold-adaptation of trypsin. *PLoS Computational Biology* **2014,** *10* (8), e1003813.
22. Santiago, M.; Ramírez-Sarmiento, C. A.; Zamora, R. A.; Parra, L. P., Discovery, molecular mechanisms, and industrial applications of cold-active enzymes. *Frontiers in Microbiology* **2016,** *7*, 1408.
23. Arcus, V. L.; Mulholland, A. J., Temperature, dynamics, and enzyme-catalyzed reaction rates. *Annual Review of Biophysics* **2020,** *49*, 163-180.

24. Vishwanath, S.; de Brevern, A. G.; Srinivasan, N., Same but not alike: Structure, flexibility and energetics of domains in multi-domain proteins are influenced by the presence of other domains. *PLoS Computational Biology* **2018,** *14* (2), e1006008.
25. Patel, D. K.; Menon, D. V.; Patel, D. H.; Dave, G., Linkers: A synergistic way for the synthesis of chimeric proteins. *Protein Expression and Purification* **2022,** *191*, 106012.
26. Papaleo, E.; Saladino, G.; Lambrughi, M.; Lindorff-Larsen, K.; Gervasio, F. L.; Nussinov, R., The role of protein loops and linkers in conformational dynamics and allostery. *Chemical Reviews* **2016,** *116* (11), 6391-6423.
27. Sonan, G. K.; Receveur-Brechot, V.; Duez, C.; Aghajari, N.; Czjzek, M.; Haser, R.; Gerday, C., The linker region plays a key role in the adaptation to cold of the cellulase from an Antarctic bacterium. *Biochemical Journal* **2007,** *407* (2), 293-302.
28. Roe, D. R.; Cheatham III, T. E., PTRAJ and CPPTRAJ: Software for processing and analysis of molecular dynamics trajectory data. *Journal of Chemical Theory and Computation* **2013,** *9* (7), 3084-3095.
29. Ding, N.; Zhao, B.; Han, X.; Li, C.; Gu, Z.; Li, Z., Starch-binding domain modulates the specificity of maltopentaose production at moderate temperatures. *Journal of Agricultural and Food Chemistry* **2022,** *70* (29), 9057-9065.
30. Shao, Q.; Jiang, Y.; Yang, Z., EnzyHTP: A high-throughput computational platform for enzyme modeling. *Journal of Chemical Information and Modeling* **2022,** *62* (3), 647-655.
31. Yang, Z.; Shao, Q.; Jiang, Y.; Jurich, C.; Ran, X.; Juarez, R. J.; Yan, B.; Stull, S. L.; Gollu, A.; Ding, N., Mutexa: A computational ecosystem for intelligent protein engineering. *Journal of Chemical Theory and Computation* **2023,** *19* (21), 7459-7477.
32. Lu, P.; Feng, M.-G., Bifunctional enhancement of a β-glucanase-xylanase fusion enzyme by optimization of peptide linkers. *Applied Microbiology and Biotechnology* **2008,** *79*, 579-587.
33. Huang, Z.; Zhang, C.; Chen, S.; Ye, F.; Xing, X.-H., Active inclusion bodies of acid phosphatase PhoC: Aggregation induced by GFP fusion and activities modulated by linker flexibility. *Microbial Cell Factories* **2013,** *12*, 1-9.
34. Hoffmann, S. M.; Weissenborn, M. J.; Gricman, Ł.; Notonier, S.; Pleiss, J.; Hauer, B., The impact of linker length on P450 fusion constructs: Activity, stability and coupling. *ChemCatChem* **2016,** *8* (8), 1591-1597.
35. Amet, N.; Lee, H.-F.; Shen, W.-C., Insertion of the designed helical linker led to increased expression of Tf-based fusion proteins. *Pharmaceutical Research* **2009,** *26*, 523-528.
36. Zhao, H. L.; Yao, X. Q.; Xue, C.; Wang, Y.; Xiong, X. H.; Liu, Z. M., Increasing the homogeneity, stability and activity of human serum albumin and interferon-α2b fusion protein by linker engineering. *Protein Expression and Purification* **2008,** *61* (1), 73-77.
37. George, R. A.; Heringa, J., An analysis of protein domain linkers: their classification and role in protein folding. *Protein Engineering* **2002,** *15* (11), 871-879.
38. Liu, C.; Chin, J. X.; Lee, D.-Y., SynLinker: an integrated system for designing linkers and synthetic fusion proteins. *Bioinformatics* **2015,** *31* (22), 3700-3702.
39. Jumper, J.; Evans, R.; Pritzel, A.; Green, T.; Figurnov, M.; Ronneberger, O.; Tunyasuvunakool, K.; Bates, R.; Žídek, A.; Potapenko, A., Highly accurate protein structure prediction with AlphaFold. *Nature* **2021,** *596* (7873), 583-589.
40. Kabsch, W.; Sander, C., Dictionary of protein secondary structure: Pattern recognition of

hydrogen-bonded and geometrical features. *Biopolymers* **1983,** *22* (12), 2577-2637.

41. Sočan, J.; Isaksen, G. V.; Brandsdal, B. O.; Åqvist, J., Towards rational computational engineering of psychrophilic enzymes. *Scientific Reports* **2019,** *9* (1), 19147.
42. Jørgensen, S.; Vorgias, C. E.; Antranikian, G., Cloning, sequencing, characterization, and expression of an extracellular α-amylase from the hyperthermophilic archaeon *Pyrococcus furiosus* in *Escherichia coli* and *Bacillus subtilis*. *Journal of Biological Chemistry* **1997,** *272* (26), 16335-16342.
43. Koch, R.; Zablowski, P.; Spreinat, A.; Antranikian, G., Extremely thermostable amylolytic enzyme from the archaebacterium *Pyrococcus furiosus*. *FEMS Microbiology Letters* **1990,** *71* (1-2), 21-26.
44. Sočan, J.; Purg, M.; Åqvist, J., Computer simulations explain the anomalous temperature optimum in a cold-adapted enzyme. *Nature Communications* **2020,** *11* (1), 2644.
45. Liu, Y.; Zhang, N.; Ma, J.; Zhou, Y.; Wei, Q.; Tian, C.; Fang, Y.; Zhong, R.; Chen, G.; Zhang, S., Advances in cold-adapted enzymes derived from microorganisms. *Frontiers in Microbiology* **2023,** *14*, 1152847.
46. Sperl, J. M.; Sieber, V., Multienzyme cascade reactions—status and recent advances. *ACS Catalysis* **2018,** *8* (3), 2385-2396.
47. Pan, S.; Ding, N.; Ren, J.; Gu, Z.; Li, C.; Hong, Y.; Cheng, L.; Holler, T. P.; Li, Z., Maltooligosaccharide-forming amylase: Characteristics, preparation, and application. *Biotechnology Advances* **2017,** *35* (5), 619-632.
48. Fields, P. A.; Somero, G. N., Hot spots in cold adaptation: localized increases in conformational flexibility in lactate dehydrogenase A4 orthologs of Antarctic notothenioid fishes. *Proceedings of the National Academy of Sciences* **1998,** *95* (19), 11476-11481.
49. Brandsdal, B. O.; Heimstad, E. S.; Sylte, I.; Smalås, A. O., Comparative molecular dynamics of mesophilic and psychrophilic protein homologues studied by 1.2 ns simulations. *Journal of Biomolecular Structure and Dynamics* **1999,** *17* (3), 493-506.
50. Papaleo, E.; Riccardi, L.; Villa, C.; Fantucci, P.; De Gioia, L., Flexibility and enzymatic cold-adaptation: A comparative molecular dynamics investigation of the elastase family. *Biochimica et Biophysica Acta (BBA)-Proteins and Proteomics* **2006,** *1764* (8), 1397-1406.
51. Pasi, M.; Riccardi, L.; Fantucci, P.; De Gioia, L.; Papaleo, E., Dynamic properties of a psychrophilic α-amylase in comparison with a mesophilic homologue. *The Journal of Physical Chemistry B* **2009,** *113* (41), 13585-13595.
52. Merlino, A.; Krauss, I. R.; Castellano, I.; De Vendittis, E.; Rossi, B.; Conte, M.; Vergara, A.; Sica, F., Structure and flexibility in cold-adapted iron superoxide dismutases: the case of the enzyme isolated from *Pseudoalteromonas haloplanktis*. *Journal of Structural Biology* **2010,** *172* (3), 343-352.
53. Truongvan, N.; Jang, S.-H.; Lee, C., Flexibility and stability trade-off in active site of cold-adapted *Pseudomonas mandelii* esterase EstK. *Biochemistry* **2016,** *55* (25), 3542-3549.
54. Isaksen, G. V.; Åqvist, J.; Brandsdal, B. O., Enzyme surface rigidity tunes the temperature dependence of catalytic rates. *Proceedings of the National Academy of Sciences* **2016,** *113* (28), 7822-7827.
55. Sočan, J.; Kazemi, M.; Isaksen, G. V.; Brandsdal, B. O.; Åqvist, J., Catalytic adaptation of psychrophilic elastase. *Biochemistry* **2018,** *57* (20), 2984-2993.

56. Koenekoop, L.; van der Ent, F.; Purg, M.; Åqvist, J., The activation parameters of a cold-adapted short chain dehydrogenase are insensitive to enzyme oligomerization. *Biochemistry* **2022,** *61* (7), 514-522.
57. Åqvist, J., Cold adaptation of triosephosphate isomerase. *Biochemistry* **2017,** *56* (32), 4169-4176.
58. Nagel, Z. D.; Cun, S.; Klinman, J. P., Identification of a long-range protein network that modulates active site dynamics in extremophilic alcohol dehydrogenases. *Journal of Biological Chemistry* **2013,** *288* (20), 14087-14097.
59. Zaragoza, J. P. T.; Offenbacher, A. R.; Hu, S.; Gee, C. L.; Firestein, Z. M.; Minnetian, N.; Deng, Z.; Fan, F.; Iavarone, A. T.; Klinman, J. P., Temporal and spatial resolution of distal protein motions that activate hydrogen tunneling in soybean lipoxygenase. *Proceedings of the National Academy of Sciences* **2023,** *120* (10), e2211630120.
60. Zhang, Z.; Jin, T.; Xie, X.; Ban, X.; Li, C.; Hong, Y.; Cheng, L.; Gu, Z.; Li, Z., Structure of maltotetraose-forming amylase from *Pseudomonas saccharophila* STB07 provides insights into its product specificity. *International Journal of Biological Macromolecules* **2020,** *154*, 1303-1313.
61. Hasegawa, K.; Kubota, M.; Matsuura, Y., Roles of catalytic residues in α-amylases as evidenced by the structures of the product-complexed mutants of a maltotetraose-forming amylase. *Protein Engineering, Design and Selection* **1999,** *12* (10), 819-824.
62. Yoshioka, Y.; Hasegawa, K.; Matsuura, Y.; Katsube, Y.; Kubota, M., Crystal structures of a mutant maltotetraose-forming exo-amylase cocrystallized with maltopentaose. *Journal of Molecular Biology* **1997,** *271* (4), 619-628.
63. Du, X.; Li, Y.; Xia, Y.-L.; Ai, S.-M.; Liang, J.; Sang, P.; Ji, X.-L.; Liu, S.-Q., Insights into protein–ligand interactions: mechanisms, models, and methods. *International journal of Molecular Sciences* **2016,** *17* (2), 144.
64. Lawson, C. L.; van Montfort, R.; Strokopytov, B.; Rozeboom, H. J.; Kalk, K. H.; de Vries, G. E.; Penninga, D.; Dijkhuizen, L.; Dijkstra, B. W., Nucleotide sequence and X-ray structure of cyclodextrin glycosyltransferase from *Bacillus circulans* strain 251 in a maltose-dependent crystal form. *Journal of Molecular Biology* **1994,** *236* (2), 590-600.
65. Broom, A.; Rakotoharisoa, R. V.; Thompson, M. C.; Zarifi, N.; Nguyen, E.; Mukhametzhanov, N.; Liu, L.; Fraser, J. S.; Chica, R. A., Ensemble-based enzyme design can recapitulate the effects of laboratory directed evolution in silico. *Nature Communications* **2020,** *11* (1), 4808.
66. Wankowicz, S.; Fraser, J., Making sense of chaos: uncovering the mechanisms of conformational entropy. *Chemrxiv* **2024**.
67. Shoseyov, O.; Shani, Z.; Levy, I., Carbohydrate binding modules: Biochemical properties and novel applications. *Microbiology and Molecular Biology Reviews* **2006,** *70* (2), 283-295.
68. Papaleo, E.; Pasi, M.; Riccardi, L.; Sambi, I.; Fantucci, P.; De Gioia, L., Protein flexibility in psychrophilic and mesophilic trypsins. Evidence of evolutionary conservation of protein dynamics in trypsin-like serine-proteases. *FEBS Letters* **2008,** *582* (6), 1008-1018.
69. Zhu, B.; Li, K.; Wang, W.; Ning, L.; Tan, H.; Zhao, X.; Yin, H., Preparation of trisaccharides from alginate by a novel alginate lyase Alg7A from marine bacterium *Vibrio* sp. W13. *International Journal of Biological Macromolecules* **2019,** *139*, 879-885.
70. Mandelman, D.; Ballut, L.; Wolff, D. A.; Feller, G.; Gerday, C.; Haser, R.; Aghajari, N.,

Structural determinants increasing flexibility confer cold adaptation in psychrophilic phosphoglycerate kinase. *Extremophiles* **2019,** *23* (5), 495-506.
71. Mirdita, M.; Schütze, K.; Moriwaki, Y.; Heo, L.; Ovchinnikov, S.; Steinegger, M., ColabFold: Making protein folding accessible to all. *Nature Methods* **2022,** *19* (6), 679-682.
72. Case, D.; Ben-Shalom, I.; Brozell, S.; Cerutti, D.; Cheatham III, T.; Cruzeiro, V.; Darden, T.; Duke, R.; Ghoreishi, D.; Gilson, M., AMBER 2019, University of California, San Francisco. **2019**.
73. Maier, J. A.; Martinez, C.; Kasavajhala, K.; Wickstrom, L.; Hauser, K. E.; Simmerling, C., ff14SB: Improving the accuracy of protein side chain and backbone parameters from ff99SB. *Journal of Chemical Theory and Computation* **2015,** *11* (8), 3696-3713.
74. Dolinsky, T. J.; Czodrowski, P.; Li, H.; Nielsen, J. E.; Jensen, J. H.; Klebe, G.; Baker, N. A., PDB2PQR: Expanding and upgrading automated preparation of biomolecular structures for molecular simulations. *Nucleic Acids Research* **2007,** *35*, W522-W525.
75. Olsson, M. H.; Søndergaard, C. R.; Rostkowski, M.; Jensen, J. H., PROPKA3: Consistent treatment of internal and surface residues in empirical p*K*a predictions. *Journal of Chemical Theory and Computation* **2011,** *7* (2), 525-537.
76. Ryckaert, J.-P.; Ciccotti, G.; Berendsen, H. J., Numerical integration of the cartesian equations of motion of a system with constraints: Molecular dynamics of *n*-alkanes. *Journal of Computational Physics* **1977,** *23* (3), 327-341.
77. Loncharich, R. J.; Brooks, B. R.; Pastor, R. W., Langevin dynamics of peptides: The frictional dependence of isomerization rates of *N*-acetylalanyl-*N'*-methylamide. *Biopolymers* **1992,** *32* (5), 523-535.
78. Miller, G. L., Use of dinitrosalicylic acid reagent for determination of reducing sugar. *Analytical Chemistry* **1959,** *31* (3), 426-428.
79. Towns, J.; Cockerill, T.; Dahan, M.; Foster, I.; Gaither, K.; Grimshaw, A.; Hazlewood, V.; Lathrop, S.; Lifka, D.; Peterson, G. D.; Roskies, R.; Scott, J. R.; Wilkins-Diehr, N., XSEDE: Accelerating Scientific Discovery. *Comput. Sci. Eng.* **2014,** *16* (5), 62-74.